Influence of Mesoscale Orography on Idealized Cold Fronts

U. SCHUMANN

DFVLR, Institute of Atmospheric Physics, D-8031 Oberpfaffenhofen, Federal Republic of Germany

(Manuscript received 31 December 1986, in final form 7 May 1987)

ABSTRACT

A three-dimensional numerical model based on the inviscid and adiabatic primitive equations in the Boussinesq approximation is used to investigate the retardation of cold fronts by high two and three-dimensional mountains, approximately the same size as the Alps. Initial and boundary conditions are specified according to an analytical model for an idealized front with constant potential vorticity. The study covers cases with uniform, neutral or stable stratification in both the cold and warm air masses. The model results are compared with previous analytical solutions of a shallow water flow model. A scale analysis and a parameter study identify the conditions under which a front is strongly influenced by mountains.

For two-dimensional cases, the study shows that the foot of the front is strongly retarded if the kinetic energy is too small to let the cold air climb over the mountain. The bulk of the front is strongly retarded if the Froude number and the relative front/mountain height are small, and if the mountain is steep. For Froude numbers of order one and for high mountains, hydraulic jumps arise in accordance with theories for layered flows. Stable stratification further enhances retardation of the front and disperses possible hydraulic jumps. In three dimensions, the front experiences deformation due to anticyclonic motion. This deformation is enhanced by stratification. The model explains the magnitude of surface-front deformation for two observed cases where cold fronts are strongly retarded at the Alps.

1. Introduction

This study examines the dynamic modification of a cold front by a mountain at scales corresponding to those of the Alps. The influence of smooth orography is considered within the framework of a three-dimensional numerical mesoscale flow model and the concept of an idealized cold front introduced by Davies (1984). The purpose of the study is to provide insight to the conditions under which a cold front experiences strong retardation and deformation.

It has long been known, e.g., see the review by Smith (1986), that cold fronts approaching the Alps from north or west may undergo severe deformation as they cross the mountains. This deformation may result in a number of important weather events including blocking and splitting of air flow on the upstream side, penetration of cold air into the northern Alpine valleys, establishment of the mistral at the western edge of the Alps and of the bora at the eastern edge, strong winds along and across the Alps, formation of gravity waves and foehn-type flows. It has also been observed, e.g., see Buzzi and Tibaldi (1978) and Pichler and Steinacker (1986), that cold fronts may trigger lee cyclogenesis in the downstream flow. Studies of frontal deformation by mountains in other regions of the world have been summarized by Smith (1986) and show qualitatively similar events.

Observations of cold fronts near the Alps have been analyzed in 1928 by Bergeron (see Godske et al., 1957)

and more recently by Buzzi and Tibaldi (1978), Steinacker (1981, 1983, 1984), Davies (1986), Blumen et al. (1986), and Hoinka (1986). Hoinka (1985) has performed a climatological study of cold fronts in central Europe and shows that cold fronts contribute a significant fraction of the precipitation in this region. Steinacker (1983) has analyzed the cold front of 2 March 1982 using data observed during the ALPEX experiment. The analysis of the front's surface isochrones is displayed in Fig. 1a and gives an example of a front which is strongly retarded and deformed by the Alps. On the other hand, cold fronts have been observed sweeping over the Alps with little deformation. For example, an analysis of the case of 4 June 1986 (see Fig. 1b) based on standard synoptic observations does not exhibit any indications of a mountain effect. It is not yet sufficiently understood which parameters are responsible for the differences.

As summarized by Davies (1984) and Bannon (1984), few theoretical/numerical studies of orographic modification of frontal motion have been undertaken. To yield some insight to the factors influencing retardation, Davies (1984) used a highly simplified cold frontal model. He employs a shallow water flow model on an f-plane in which a "free surface" represents the interface between cold air below and warm air above. The cold air is modeled as a homogeneous, inviscid, incompressible fluid. The flow of the cold air layer is driven by a reduced gravity and a constant imposed geostrophic pressure gradient. For constant potential
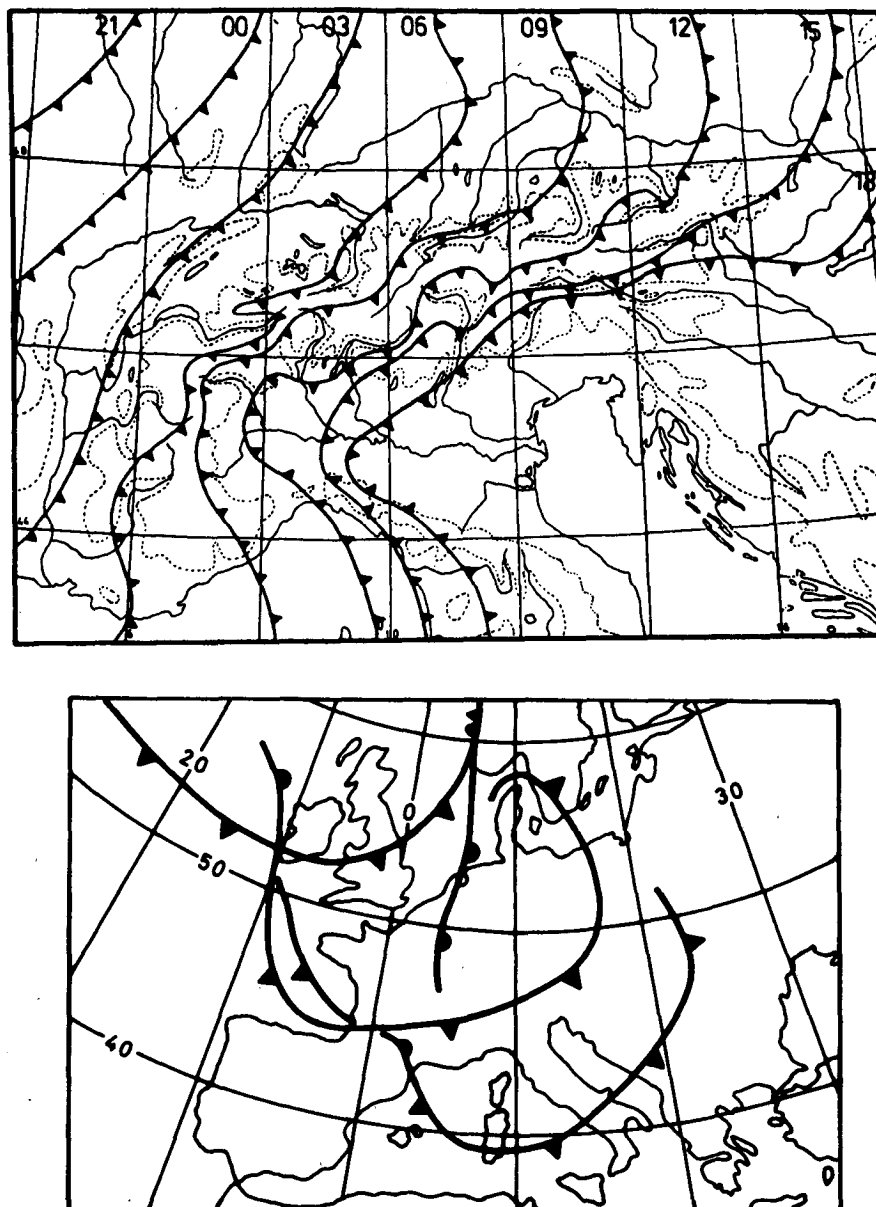
FIG. 1. Surface isochrones of a cold front passing around and over the Alps. (a) Top: from 2100 UTC 1 March to 1800 UTC 2 March 1982; analysis due to Steinacker (1983). (b) Bottom: At 1200 UTC for 3–5 June 1986.

vorticity, and assuming semigeostrophic equilibrium, Davies deduced an analytical solution for the front moving over a two-dimensional mountain ridge. The character of this solution is determined by two dimensionless characteristic numbers, viz. a rotational Froude number and a front–mountain aspect ratio. As a consequence of the semigeostrophic approximation, the solution is physically realistic only if the front–mountain aspect ratio is larger than a certain value that depends on the rotational Froude number.

Haderlein (1986, personal communication) has considered the same case by solving numerically the shallow water equations without making the semigeostrophic assumption. If the flow velocity normal to the front is small in comparison to the wave speed of gravity waves, his results agree with the analytical solution of Davies (1984). For larger velocities some of his solutions indicate a tendency to form a hydraulic jump at the upstream side of the ridge. Haderlein further studied two-dimensional shallow water flow over circular or elliptical mountains. The model results have not yet been compared with observed cases.

The study of Davies (1984) is restricted to neutral stratification and a quasi-stationary front. Bannon

(1984) has considered the effect of orography on front-ogenesis in stably stratified atmosphere. His theory is restricted to semigeostrophic motions and a linearized surface boundary condition, which is only valid for low mountains. Bannon found that the cold front is retarded on the upslope of the mountain, with a maximum retardation amounting to half the mountain height times the ratio of Brunt–Väisälä frequency to the Coriolis frequency. The effect of stratification on fronts over high and mesoscale mountains has not yet been analyzed.

The analyses by Davies, Haderlein and Bannon concentrate on the transient flow of a cold front across a mountain (as does the present study). But when the front has passed the mountain ridge, the flow over the mountain itself becomes quasi-stationary after some time and resembles the upstream effects that accompany the impulsive initiation of stratified flow over a mountain ridge. For nonlinear shallow layered fluid flow, Long (see the review in Long, 1972), and Houghton and Kasahara (1968) have shown that hydraulic jumps arise if the gravitational Froude number lies within a certain range of order one. Baines (1980) used the concept of hydraulic blocking described by this theory to develop a simple dynamical model, which explains the southerly buster observed in Australia, in terms of a gravity current trapped by a mountain ridge perpendicular to the frontal line of a shallow cold front. The effect of Coriolis forces on the generation of hydraulic jumps has been discussed by Houghton (1969) and Williams and Hori (1970). Pierrehumbert and Wyman (1985) studied uniformly stratified fluid flow over a mountain ridge initiated suddenly from rest. Frontal motion across mountains has not yet been discussed in terms of such concepts.

In this paper a model is described, which is still rather simple but sufficient to explain the essential mechanisms of observed retardation of cold fronts at high mountains. In the model, the scales of the mountain represent the Alps but the orography is much smoother than in reality. These scales require a mesoscale model because they are too small to be described quasi-geostrophically but are approximately in hydrostatic equilibrium. The frontal model corresponds to that of Davies (1984) in that his analytical solution is taken to specify initial and boundary conditions. Aspects of frontogenesis and lee cyclogenesis are beyond the scope of the present study. The model is first applied to flows with homogeneous air masses. Then the effect of stratification and three-dimensional mountains is included because this is necessary to explain observations. The numerical model and its initialization are described in section 2.

The questions to be discussed are:

• which nondimensional parameters control the character of the mountain's influence on the simplified cold front?

• how do the solutions of the present model compare with Davies' results and what are the reasons for the differences?

• which changes are to be expected from stratification for nongeostrophic flow over high mountains?

• what are the effects of three-dimensional mountains compared to two-dimensional ones?

• does the model explain the main characteristics of observed frontal deformations?

These questions are addressed in sections 3 to 7 and the answers are summarized in section 8.

2. The mathematical model

This section describes the mathematical model and its numerical implementation. Since initial and boundary values are specified according to Davies (1984) we start with a brief summary of the details of his model as far as necessary for the present study. Thereafter, the basic equations and their numerical treatment are reported.

a. Davies' model

The flow situation considered is sketched in Fig. 2. A "free surface" $h(x, t)$ represents the front's interface. The height of the front at infinity ($x \rightarrow -\infty$) is H_F. The cold air is assumed to have uniform density ρ_0 and flows with vertically uniform velocity u normal to the front in x-direction and v parallel to the front in y-direction. The constant temperature θ of the cold air differs from the temperature θ_0 of the overlying warm air by $\Delta\theta$ so that $g' = g\Delta\theta/\theta_0$ is the effective reduced gravity. The Coriolis frequency f and the geostrophic wind components of the warm air mass U and V are constants. For constant potential vorticity $(f + \partial v/\partial x)/h \approx f/H_F$ the front moves quasi-stationarily over flat terrain with the geostrophic wind U in the horizontal direction normal to the front; the height of the front (Davies, 1984) is
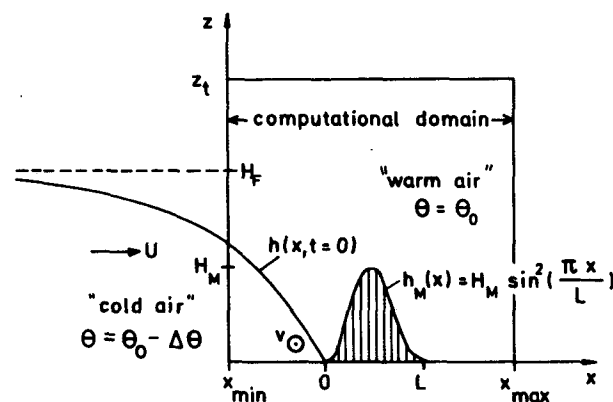

FIG. 2. Schematic sketch of the idealized cold front approaching a two-dimensional mountain ridge.

$$h(x, t) = H_F\{1 - \exp[(x - Ut)/R]\}, \quad x - Ut \leqslant 0. \quad (1)$$

Here

$$R = \frac{C}{f}, \quad C = \sqrt{g'H_F} \quad (2)$$

are the Rossby radius and the gravity wave speed, respectively. Over flat terrain, the velocity v along the front is $v = V$ in the warm air and

$$v(x, t) = V - C \exp[(x - Ut)/R], \quad x - Ut \leqslant 0 \quad (3)$$

in the cold air. Davies has considered this wedge of cold air approaching an infinitely long orographic ridge with height profile

$$h_M(x) = \begin{cases} H_M \sin^2(\pi x/L), & 0 \leqslant x \leqslant L \\ 0, & \text{elsewhere} \end{cases} \quad (4)$$

where L is the width and H_M the height of the mountain.

The shallow water equations in two dimensions for the horizontal velocity $\mathbf{v} = (u, v)^T$ and the height of the free surface h above ground are

$$\frac{\partial u}{\partial t} + \mathbf{v} \cdot \nabla u = -g' \frac{\partial}{\partial x}(h + h_M) + f(v - V), \quad (5)$$

$$\frac{\partial v}{\partial t} + \mathbf{v} \cdot \nabla v = -g' \frac{\partial}{\partial y}(h + h_M) - f(u - U), \quad (6)$$

$$\frac{\partial h}{\partial t} + \nabla \cdot (\mathbf{v}h) = 0. \quad (7)$$

Davies (1984) considers the one-dimensional case and applies the semigeostrophic approximation in which the acceleration $du/dt = \partial u/\partial t + \mathbf{v} \cdot \nabla u$ is neglected in comparison to other horizontal accelerations. He deduces an analytical solution for the height of the front's interface $h(x, t)$. If $(H_F L)/(H_M R)$ is less than a value close to π, this solution results in nonreal negative values for $h(x, t)$ near the tip of the front.

b. The three-dimensional numerical model

A preliminary description of the numerical model and the solution method (the "MESOSCOP" program) has been given by Schumann and Volkert (1984) and Volkert and Schumann (1986). In many respects, the method follows the proposals of Clark (1977). The main features are summarized.

Except for buoyancy, the model treats constant density fluid flow according to the Boussinesq approximation. Frictional forces are intentionally neglected for the present application in order to reduce the number of independent parameters. The method integrates the dynamic equations for the three velocity components $\mathbf{v} = (u, v, w)^T$ and two conservation equations, one for potential temperature θ and one for a passive scalar ψ. For stably stratified air flow, the model actually computes the temperature difference $\theta' = \theta(x, y, z)$

$- \bar{\theta}(z)$, and ψ is used as a tracer to distinguish between warm and cold air masses. The variable p denotes the deviation from the initial warm air pressure distribution where U and V are the geostrophic wind components. The respective equations are

$$\nabla \cdot \mathbf{v} = 0, \quad (8)$$

$$\frac{\partial \mathbf{v}}{\partial t} + \mathbf{v} \cdot \nabla \mathbf{v} = -\frac{1}{\rho_0} \nabla p + \mathbf{c} + \frac{\theta' \mathbf{g}}{\theta_0}, \quad (9)$$

$$\mathbf{c} = f(v - V, U - u, 0)^T, \quad \mathbf{g} = (0, 0, g)^T, \quad (10)$$

$$\frac{\partial \theta'}{\partial t} + \mathbf{v} \cdot \nabla \theta' + w \frac{d\bar{\theta}}{dz} = 0, \quad (11)$$

$$\frac{\partial \psi}{\partial t} + \mathbf{v} \cdot \nabla \psi = 0. \quad (12)$$

Terrain-following coordinates are used to represent orography. The computational domain extends vertically up to $z = z_t$. In most cases (unless specified otherwise) $z_t = 1.5H_F$; this value has been found to be large enough to avoid disturbances from the top boundary. The horizontal limits can be identified from the plots depicting the results. The limits are intended to be sufficiently large so that reflections at these boundaries are of small importance.

The numerical method employs second-order finite-difference approximations in space for advection of momentum. Advection of temperature is treated with a second-order upwind scheme proposed by Smolarkiewicz (1984). The pressure is determined from a Poisson equation in order to satisfy the continuity equation. The computational domain is equidistantly divided into finite grid cells. In all two-dimensional cases the horizontal grid spacing is $L/32$ (the number of grid points is 64 or 96 depending on the lateral limits of the computational domain), the vertical grid width is $z_t/40$. Test runs have shown that doubling the grid spacings diffuses the fields near the frontal interface more strongly but still gives essentially the same results. Therefore, in three dimensions larger grid intervals are taken (as specified below) in order to limit the computational work. Numerical stability limits the time step Δt according to a Courant condition. Since the maximum vertical velocity is not known from the initial conditions, we set $\Delta t = 0.1\Delta x/\max(U, C)$ where Δx is the horizontal grid spacing.

The top boundary condition assumes the radiative boundary condition according to Bougeault (1983) and Klemp and Durran (1983). For neutral stratification this condition implies constant pressure at the top surface. Initial conditions and boundary conditions at the inflow boundary are set according to the analytical solution of Davies (1984). This means we set $u = U$ and

$$\varphi = \gamma \varphi_C + (1 - \gamma)\varphi_W \quad (13)$$

for $\varphi = (v, \theta', \psi)$, where φ_C is the value valid for $z < h(x, t)$ in the cold air and φ_W the value for $z > h(x,$

t) in the warm air. Here v_C is given by Eq. (3), and v_W = V, $\theta'_C = \psi_C = \theta_0 - \Delta\theta$, $\theta'_W = \psi_W = \theta_0$. In principle, the weight $\gamma = \gamma(x, z, t)$ is unity in the cold air, and zero above. However, in the finite-difference grid this would imply a stepwise profile of the interface so that $\partial h/\partial x$ is zero for some distance and then very large at the locations where the height steps by one vertical grid interval. This discontinuous behavior results in a local imbalance between horizontal gradients of the hydrostatic pressure and Coriolis forces which causes spurious motions. In order to overcome this problem we use a value of γ which interpolates between the theoretical values near the interface over one grid interval according to

$$\gamma_k = \min\{1, \max[0, (h(x, t) - z_{k-1/2})/\Delta z_k]\}, \quad (14)$$

where $z_{k-1/2}$ is the height of the mesh cell boundary between grid points with indices k and $k - 1$, and Δz_k = $z_{k+1/2} - z_{k-1/2}$ is the vertical mesh spacing. The initial field is adjusted by a solution of a Poisson equation in order to make it nondivergent.

At the outflow boundary, a radiation condition of Sommerfeld-type is employed. Since this boundary is sufficiently far downstream of the front for all cases, details of this boundary condition do not matter. For three-dimensional simulations periodic boundaries are assumed at the lateral sides for all results shown in the figures. Test runs with open boundaries have confirmed that the lateral boundary does not significantly influence the results.

The initial conditions and the boundary conditions at the inflow side impose discontinuities on the v-velocity (this velocity jumps from V to $V - C$ at the tip of the front) and the temperature field (jump by $\Delta\theta$). These discontinuities cannot be represented exactly by the finite-difference scheme. Instead they are initially distributed over two grid cells, and are spread over a few more grid cells during the course of integration. Therefore, tests must be made to ensure that these approximation errors do not cause the results to deteriorate. Figure 3 displays such test results for a two-dimensional front propagating on a plane. The parameters are taken in accordance with the parameters of the case P0, see Table 2 (which forms the reference case for a parameter study reported below), but H_M = 0. Isotherms at initial and late time are plotted where the surface front has left the right boundary of the computational domain ($t^* = tU/L$). The spreading of the contour lines is a measure of the numerical diffusion. Figure 3 also contains the contours of constant v-velocity at the late time. The velocity difference between the cold and warm air is negative and increases in magnitude from zero to the value C at the front's tip. The related Coriolis force just balances the hydrostatic pressure gradient at the surface. The exact solution according to Eq. (1) is included for comparison. We see that the numerical scheme describes the advection of the temperature field with very little numerical diffusion. This demonstrates that the Smolarkiewicz scheme is particularly suited for this purpose. The errors in the advection of momentum due to the second-order central differences are somewhat larger, but still acceptable. The zig-zag contours for the velocity v are consequences of the approximation of the curved frontal interface in the finite-difference scheme at initial time and at the inflow boundary. Obviously, these approximation errors are of negligible importance with respect to the resultant frontal interface.

3. Scale analysis

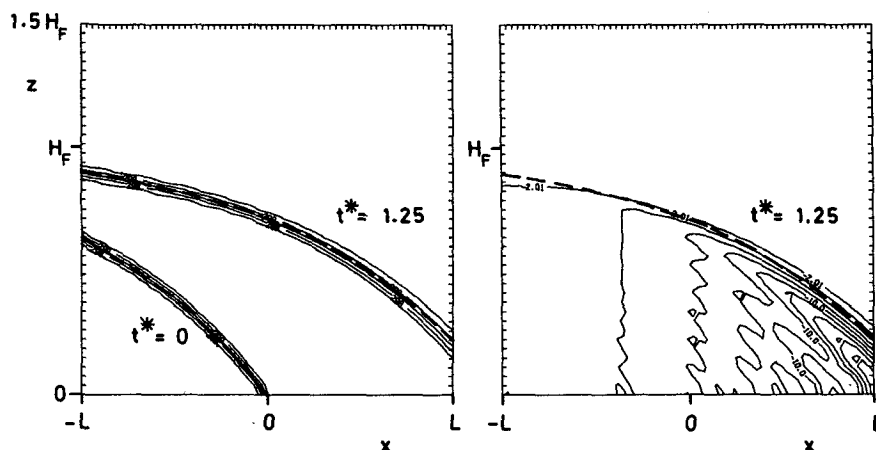The independent dimensional parameters of Davies' model are

FIG. 3. Propagation of a front for case P0 without mountains. Left: Isotherms at times $t^* = tU/L = 0$ and 1.25 in comparison to the exact solution (dashed curve). Several isotherms with increments $\Delta\theta/6$ represent the frontal interface. Right: Contours of the velocity v (increment $C/10$) parallel to the front at time $t^* = 1.25$.

H_M, L, H_F, U, V, f and g'.

Thus, dimensional analysis suggests that five independent, nondimensional characteristic numbers can be formed. One possible set of characteristic numbers is $\epsilon = L/R$, the rotational Froude number; $H = H_F/H_M$, the height aspect ratio; $F = U/C$, the (gravitational) Froude number; $G = H_M/L$, the mountain slope; and $W = V/U$, the velocity ratio. Here C and R are as defined in Eq. (2). We will see that other combinations of characteristic numbers as given in Table 1 might be informative, as well. For stratified flow, the Brunt–Väisäilä frequency, $N = (g\theta_0^{-1}d\bar{\theta}/dz)^{1/2}$, and in three dimensions the horizontal length scale L_y of the mountain in y-direction, are additional parameters from which we form the (inverse) stratification Froude number $F_N = NH_M/U$ and the scale ratio $M = L/L_y$.

Not all of the characteristic numbers are equally important. Subsequently, scale analysis is used to identify the characteristic numbers which are relevant for the interaction of a cold front with orography. For this purpose, first the shallow water equations for flow over a mountain ridge and then the full three-dimensional nonhydrostatic equations are investigated.

a. Shallow water flow over a mountain ridge

We introduce nondimensional variables (denoted by an overbar) that are of order unity:

$$u = U\bar{u}, \quad v - V = C\bar{v}, \quad x = L\bar{x}, \quad y = L_y\bar{y},$$

$$t = \bar{t}L/U, \quad h = H_F\bar{h}, \quad h_M = H_M\bar{h}_M. \tag{15}$$

The grouping $v - V = C\bar{v}$ is suggested by Eq. (3) and used instead of $v = C\bar{v}$ because this eliminates the influence of V if the flow is independent of the y-coordinate. Substituting (15) into Eqs. (1)–(7) yields the following system:

$$\bar{h} = 1 - \exp[(\bar{x} - \bar{t})\epsilon], \quad \bar{x} - \bar{t} \leqslant 0, \tag{16}$$

$$\bar{v} = -\exp[(\bar{x} - \bar{t})\epsilon], \quad \bar{x} - \bar{t} \leqslant 0, \tag{17}$$

$$\bar{h}_M = \sin^2(\pi\bar{x}), \quad 0 \leqslant \bar{x} \leqslant 1; \quad \bar{h}_M = 0, \quad \text{elsewhere}, \tag{18}$$

$$F^2\left\{\frac{\partial\bar{u}}{\partial\bar{t}} + \bar{u}\frac{\partial\bar{u}}{\partial\bar{x}}\right\} = -\frac{\partial\bar{h}}{\partial\bar{x}} - \frac{1}{H}\frac{\partial\bar{h}_M}{\partial\bar{x}} + \epsilon\bar{v}, \tag{19}$$

$$\frac{\partial\bar{v}}{\partial\bar{t}} + \bar{u}\frac{\partial\bar{v}}{\partial\bar{x}} = \epsilon(1 - \bar{u}), \tag{20}$$

$$\frac{\partial\bar{h}}{\partial\bar{t}} + \frac{\partial(\bar{u}\bar{h})}{\partial\bar{x}} = 0. \tag{21}$$

Several conclusions can be drawn from these equations: As a consequence of the hydrostatic equilibrium implied by the shallow water equations, the shallow water flow is independent of the steepness $G = H_M/L$ of the mountain. The motion of the front is also in-

TABLE 1. Nondimensional characteristic numbers.

Rotational Froude number:	$\epsilon = L/R$
Height aspect ratio:	$H = H_F/H_M$
(Gravitational) Froude number:	$F = U/C$
Mountain slope:	$G = H_M/L$
Velocity ratio:	$W = V/U$
(Inverse) stratification Froude number:	$F_N = \dfrac{NH_M}{U}$
Horizontal scale ratio:	$M = L/L_y$
Rossby number:	$\text{Ro} = \dfrac{F}{\epsilon} = \dfrac{U}{fL}$
Ratio of inertia relative to Coriolis forces:	$N_1 = \dfrac{F^2}{\epsilon} = \dfrac{U^2R}{C^2L}$
Ratio of kinetic to potential energy:	$N_2 = \dfrac{1}{2}F^2H = \dfrac{U^2}{2g'H_M} = \dfrac{U^2H_F}{2C^2H_M}$
Same as N_2 for stable stratification:	$N'_2 = \dfrac{1}{2}[(F^2H)^{-1} + F_N^2]^{-1} = \dfrac{1}{2}\dfrac{U^2}{g'H_M + N^2H_M^2} = \dfrac{N_2}{1 + N_5}$
Ratio of mountain/frontal steepness:	$N_3 = \dfrac{1}{H\epsilon} = \dfrac{H_MR}{H_FL}$
Measure for importance of non-hydrostatic accelerations:	$N_4 = F^2G^2H = \dfrac{U^2H_M}{g'L^2}$
Measure for importance of uniform stratification:	$N_5 = F_N^2F^2H = \dfrac{N^2H_M}{g'}$

dependent of the velocity ratio $W = V/U$ in the present case where the surface front is parallel to the mountain ridge. The acceleration $d\bar{u}/d\bar{t}$ is small in comparison to other accelerations in direction normal to the front, i.e., the flow is semigeostrophic, if

$$N_1 = F^2/\epsilon \quad \text{and} \quad N_2 = \tfrac{1}{2}F^2H \qquad (22)$$

are both much smaller than unity. (The factor ½ is included so that N_2 denotes the ratio of kinetic and potential energy, as discussed in section 4.) The flow gets geostrophic in both velocity components if in addition, $\epsilon \gg 1$. The slope of the front $\partial \bar{h}/\partial \bar{x}$ is of order ϵ, the mountain slope $H^{-1}\partial \bar{h}_M/\partial \bar{x}$ is of order π/H; thus, the steepness of the front is small in comparison to that of the mountain if

$$N_3 = (\epsilon H)^{-1} \leqslant \pi^{-1}. \qquad (23)$$

In fact, Davies' solution is strictly valid only if all three characteristic numbers, N_1, N_2, N_3 are small. It is independent of the Froude number $F = U/C$.

b. Three-dimensional stratified flow

Equations (8)–(11) together with their initial and boundary conditions in terms of Eqs. (1)–(4) can be turned into a nondimensional set of equations for variables of order unity by introducing

$$u = U\bar{u}, \quad v - V = C\bar{v}, \quad w = \bar{w}UH_M/L, \quad \bar{\mathbf{v}} = (\bar{u}, \bar{v}, \bar{w})^T,$$

$$x = L\bar{x}, \quad y = L_y\bar{y}, \quad z = H_F\bar{z}, \quad t = \bar{t}L/U,$$

$$p = \rho_0 C^2 \bar{p}, \quad \theta' = \Delta\theta\bar{\theta}', \quad h = H_F\bar{h}, \quad h_M = H_M\bar{h}_M. \qquad (24)$$

The scaling of w accounts for the vertical velocity induced by horizontal flow over the mountain profile. The scale of the pressure incorporates the hydrostatic surface pressure deviation $\rho_0 g' H_F = \rho_0 C^2$ far upstream in the cold layer. The reference scales resemble the scales of a given front approaching a mountain of comparable height ($H_F \approx H_M$) driven by large temperature differences $\Delta\theta$ (large values of g'). For strongly stable stratification ($N^2H_F \gg g'$), for strongly rotating flows ($fLU/H_F \gg g'$) or for mountain flows without a front ($H_F \ll H_M$) other reference scales, e.g., those used by Pierrehumbert and Wyman (1985), would be more appropriate. The present selection suits the idealized front concepted by Davies (1984) and its modifications by mesoscale orography and moderate stratification. The resultant nondimensional equations read

$$\bar{\nabla} \cdot \bar{\mathbf{v}} = 0, \qquad (25)$$

$$\frac{\partial \bar{\mathbf{v}}}{\partial \bar{t}} + \bar{\mathbf{v}} \cdot \bar{\nabla}\bar{\mathbf{v}} + WM\frac{\partial \bar{\mathbf{v}}}{\partial \bar{y}} = \begin{cases} -F^{-2}\partial\bar{p}/\partial\bar{x} + \dfrac{\epsilon}{F^2}\bar{v} \\[2mm] -MF^{-1}\partial\bar{p}/\partial\bar{y} + \epsilon(1 - \bar{u}) \\[2mm] (F^2G^2H)^{-1}(-\partial\bar{p}/\partial\bar{z} + \bar{\theta}'), \end{cases}$$

$$(26)$$

$$\frac{\partial \bar{\theta}'}{\partial \bar{t}} + \bar{\mathbf{v}} \cdot \bar{\nabla}\bar{\theta}' + WM\frac{\partial \bar{\theta}'}{\partial \bar{y}} = -F_N^2 F^2 H\bar{w}, \qquad (27)$$

where

$$\bar{\nabla} = \left(\frac{\partial}{\partial\bar{x}}, MF^{-1}\frac{\partial}{\partial\bar{y}}, H^{-1}\frac{\partial}{\partial\bar{z}}\right)^T. \qquad (28)$$

Thus, in contrast to the two-dimensional case, $W = V/U$ does influence the three-dimensional flow state. Its effect is weighted by the scale ratio $M = L/L_y$. Also, the steepness of the mountain $G = H_M/L$ arises formally, but its effect is small in the hydrostatic limit where

$$N_4 = F^2G^2H \ll 1. \qquad (29)$$

Vertical motion in stratified fluid causes large temperature changes if

$$N_5 = F_N^2 F^2 H \qquad (30)$$

is large. If both numbers, N_4 and N_5, are small, then the shallow water equations become valid approximations. In general, however, the three-dimensional stratified flow is controlled by seven independent characteristic numbers, e.g. F, ϵ, H, W, M, G and F_N or combinations thereof (see Table 1).

4. Influence of orography on cold fronts in two dimensions

Scale analysis identifies which forces are important but does not tell us how these forces affect the flow. Subsequently, the influence of a sinusoidal mountain on the idealized cold front is investigated by means of a parameter study. In this section, we discuss two-dimensional flows with neutral stratification in both the warm and cold air masses.

For this purpose, cases are considered which differ from a reference case in just one dimensional parameter. The reference case P0 is selected such that all forces, i.e. those due to horizontal inertia, hydrostatic pressure gradient and Coriolis forces, are of comparable magnitude. Hence, the rotational Froude number ϵ and the Froude number F are unity. Moreover, the frontal/mountain aspect ratio H, the mountain slope G, and the reference scales (e.g., L and U) are chosen to represent meteorological fronts as they are typically observed approaching the Alps (Hoinka, 1985). At these scales the flow is effectively in hydrostatic equilibrium ($N_4 \leqslant 0.0032$). The actual parameters are listed in Table 2. The parameters are varied by factors of 2 or 4 in order to get large differences. Cases P1 and P2 show the effect of varying the horizontal velocity in x-direction. In case P3 the temperature difference, which determines the reduced gravity g', is enlarged. In cases P4, P5, and P6 geometrical parameters are varied. In case P7 the Coriolis frequency f has been doubled; this value—although somewhat larger than found on earth—is taken to make case P7 significantly different from P0.

Both Davies' model and the numerical model described in section 2 are applied to identify the differ-

TABLE 2. Parameters of two-dimensional cases. A blank entry denotes the same value as in the first line.
In all cases: $g = 10$ m s^{-2}, $\theta_0 = 300$ K, $\rho_0 = 1.2$ kg m^{-3}, $N = 0$.

	Physical parameters								
Case	H_M (km)	L (km)	H_F (km)	$\Delta\theta$ (K)	U (m s^{-1})	V (m s^{-1})	$10^4 f$ (s^{-1})	C (m s^{-1})	R (km)
P0	2	200	4	3	20	0	1	20	200
P1					40				
P2					5				
P3				12				40	400
P4		50							
P5	0.5								
P6			1					10	100
P7							2		100

	Nondimensional numbers								
	ϵ	H	F	G	N_1	N_2	N_3	$10^5 N_4$	Ro
P0	1	2	1	0.01	1	1	0.5	20	1
P1		2			4	4		80	2
P2			0.25		0.0625	0.0625		1.25	0.25
P3	0.5		0.5		0.5	0.25	1	5	
P4	0.25			0.04	4		2	320	4
P5		8		0.0025		4	0.125	5	
P6	2	0.5	2		2		1		
P7	2				0.5		0.25		0.5

ences. Figure 4 displays the results of Davies' model and Fig. 5 the results of the numerical model in terms of the isochrones of the interface between the cold and warm air masses at a sequence of nondimensional times $t^* = tU/L$. Subsequently, first the semigeostrophic results from Davies' model and then the results from the numerical model are discussed.

a. Semigeostrophic results from Davies' model

Davies' analytical solution is independent of the Froude number F, and this explains why cases P0, P1, and P2, which differ only by the amount of the velocity U, give identical results in nondimensional coordinates. As discussed by Davies (1984), the retardation is strong if $N_3 = (H\epsilon)^{-1}$ is large. For $N_3 > \pi^{-1}$, i.e., for cases P0, P3, P4 and P6, the solutions break down at a critical nondimensional time t_c^* in that the front's interface undercuts the mountain profile. The values of t_c^* and the related position x_c of the surface front are $t_c^* = (0.912, 1.392, 2.383, 1.123)$, $x_c/L = (0.569, 0.529, 0.514, 0.486)$, for cases P0, P3, P4, P6, respectively. For $N_3 < \pi^{-1}$, cases P5 and P6, the retardation is less pronounced and the surface front succeeds to cross the whole mountain ridge. The analytical solution of Davies is restricted, however, to the time period where the surface front has not yet passed the downstream side of the mountain. For this reason, solutions for $t^* > 1$ are not plotted in these cases. As noted by Davies (1984), the front is retarded on the upstream side and accelerated on the downstream side of the mountain. It appears that this effect is mainly

of geometric origin in that the volume of cold air displaced by the mountain is spread horizontally. The disturbance induced by the mountain spreads upstream over a distance of order R, the Rossby radius. This can be seen by comparing the sequence of cases P4, P3, P0, and P7 for which the values of $\epsilon = L/R$ increase from 0.25 to 2 while the height ratio $H = H_F/H_M = 2$ remains constant.

b. Nongeostrophic results from the numerical model

The results from the numerical model, which does not assume semigeostrophic equilibrium, are depicted in Fig. 5. As identified in section 3, both the characteristic numbers N_1 and N_2 have to be small to admit the semigeostrophic approximation. For the cases considered, these numbers are smallest for case P2 ($N_1 = N_2 = 0.0625$). In fact, the results of both methods exhibit only small differences for case P2 (see Fig. 5). For all other cases, at least one of the two numbers is not small and this explains why the two methods give large differences in most cases. In the following the results are interpreted in terms of elementary physical processes and order of magnitude estimates.

1) CONVERSION OF KINETIC INTO POTENTIAL ENERGY

The cold air mass arrives at the mountain with specific kinetic energy $U^2/2$ per unit mass. For small Coriolis forces (large values of N_1) this kinetic energy is converted into potential energy. In order to climb over
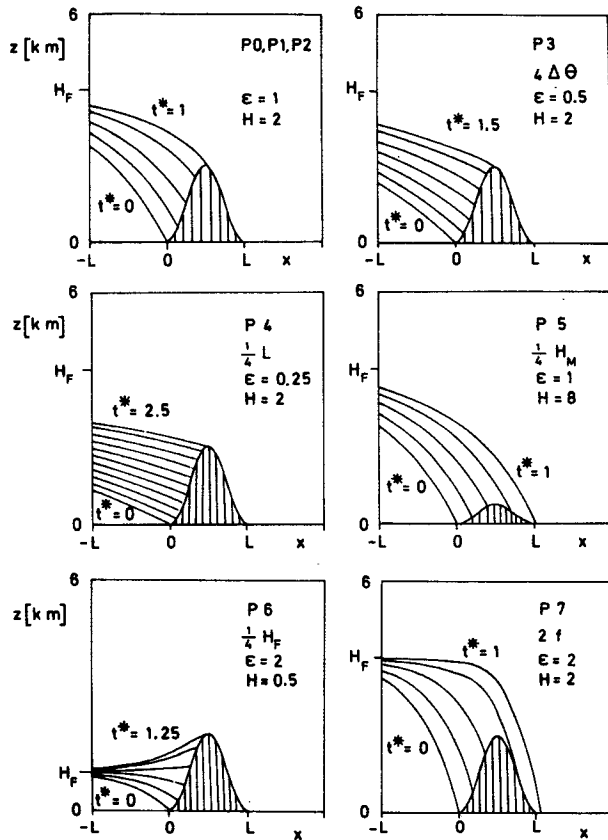
FIG. 4. Semigeostrophic results from Davies' (1984) analytical solutions in terms of isochrones of the frontal interface at times t^* = tU/L = 0, 0.25, 0.5, ... ; P0 is the reference case; P0, P1 and P2 give identical results. In all other cases, one of the dimensional parameters is changed as indicated (e.g., $\Delta\theta$ has been quadrupled in case P3). H_F denotes the height of the front at infinity, L the width of the mountain ridge. The values of the rotational Froude number ϵ, and the height ratio H are as indicated.

the mountain, the foot of the front has to gain a potential energy $g'H_M$. If

$$N_2 = \frac{U^2}{2g'H_M} = \frac{U^2 H_F}{2C^2 H_M} = \frac{1}{2}F^2 H \qquad (31)$$

is less than one, the foot of the cold front will be retarded because it lacks sufficient kinetic energy. This is exemplified by cases P2 and P3 (see Table 2 and Fig. 5). On the other hand, P1 and P5 are examples where the kinetic energy is large enough to lift the cold air over the mountain.

If the kinetic energy is small ($N_2 < 1$) the front is retarded until advected cold air replaces the warm air on the windward side of the mountain. Cold air at great heights needs only a little or no additional energy to flow over the mountain. Thus, at times greater than R/U, the front is retarded only a little if the height ratio H is large. If, however, both N_2 and H are small then a total blocking is to be expected. Such a blocking is indicated in Fig. 5 for case P3 in the initial period,

while the height of the front at the foot of the mountain is small.

Once the cold air is lifted up to the mountain crest it is accelerated by gravity down the mountain slope. For $F < 1$ we observe downslope velocities which are much larger than the initial velocity U (e.g., see case P2). This is a sort of bora effect with strong downdrafts within the cold air.
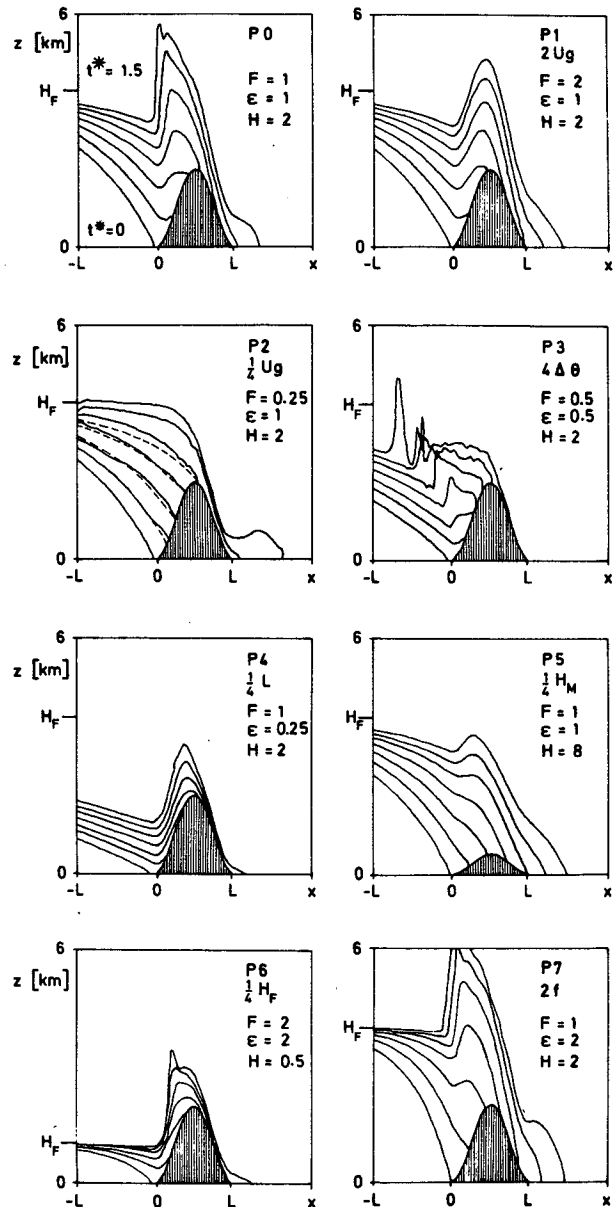

FIG. 5. Nongeostrophic two-dimensional numerical results in terms of isochrones of the frontal interface at times t^* = tU/L = 0, 0.25, ..., 1.5. P0 is the reference case. In all other cases, one of the dimensional parameters is changed as indicated (e.g., U has been doubled in case P1). The values of the Froude number F, the rotational Froude number ϵ, and the height ratio H are as indicated. For case P2, the semigeostrophic solution is given by dashed curves for $t^* \leq 1$.

2) SPREADING OF DISTURBANCES BY GRAVITY WAVES

Plane waves with wave number K in a shallow layer of depth H spread relative to the fluid with a wave speed $c = [g'h + f^2/K^2]^{1/2}$ (Pedlosky, 1987, p. 73). For short waves ($K \gg 1/L$, as for those waves which are excited when the front just reaches the mountain or which form at hydraulic jumps) or for small rotational Froude number ϵ, the effective wave speed is $c = (g'h)^{1/2}$. This wave speed approaches the value C far upstream in the cold layer. Thus, we expect very different behavior in cases with Froude numbers $F = U/C$ larger or smaller than unity. If $F > 1$, short-wave disturbances induced by the mountain cannot propagate upstream. This is typically observed in cases P1 and P6 (see Fig. 5). On the other hand, if $F < 1$, disturbances induced by the mountain do spread upstream. This effect can be seen in cases P3 and P2. In the latter case, C is much larger than U and the disturbances reach the inflow boundary of the computational domain rather early. In cases P0 and P3 a hydraulic jump arises at positions where $c = U$. On the lee side, the downslope wind, which results from the conversion of potential into kinetic energy, creates a second hydraulic jump if the local flow velocity exceeds the wave speed c. See, for example, cases P2 and P7.

3) EFFECT OF CORIOLIS FREQUENCY

The effect of the Coriolis frequency f is twofold: First, it influences the Rossby radius and thus the initial conditions for the present model-front. Second, for large Coriolis forces the flow approaches the semigeostrophic state discussed in section 4.a. Case P7 illustrates the effect of doubling the Coriolis frequency. Obviously, the Coriolis force is not large enough in this case to enforce semigeostrophic equilibrium, and the main effect of Coriolis forces comes from the changed initial condition. Due to the reduced Rossby radius, the front is steeper in case P7 than in case P0. Hence, the cold air replaces the warm air on the upstreamside of the mountain more quickly.

4) FORMATION OF HYDRAULIC JUMPS AFTER LONG TIMES

The numerical simulations show that hydraulic jumps are forming, which was not to be expected from the results of Davies (1984). Further, case P3 exhibits oscillations which require further explanations.

The present study concentrates on the initial period of flow of a shallow layer of cold air over a mountain for $t \leq 1.5L/U$. A quasi-stationary flow state is to be expected for times much longer than $\max(R, L)/U$ because the front has traveled far downstream of the mountain. Although the present numerical results are still nonstationary, some features of the results can be understood by comparing them with theories on stationary flows.

A shallow layer of inviscid fluid flowing at constant speed over a mountain can create hydraulic jumps. Figure 6, based on Houghton and Kasahara (1968), maps regimes with and without jumps as a function of the Froude number Fr and the height ratio $H_M/H_F = H^{-1}$. The stationary theory predicts the formation of jumps in pairs, one upstream and one downstream of the ridge. Our transient simulations show that the upstream jump is created first and then the downstream one appears.

The map is strictly valid only for nonrotating flows ($f = 0$). No equivalent theory exists for flows over mountains in a rotating system. Houghton (1969) and Williams and Hori (1970) consider the transient motion of a shallow water layer on an f-plane without mountains starting from an initial velocity disturbance of magnitude U over a length L. They find that Coriolis forces tend to reduce the amplitude of a hydraulic jump and to delay its formation but apparently do not totally suppress its formation. The reduction of hydraulic jumps by Coriolis forces can be explained as follows: Behind the upstream hydraulic jump the velocity u is less than U. As a consequence, the flow downstream the jump experiences positive acceleration in y-direction (see Eq. 6). This in turn causes acceleration in x-direction (see Eq. 5) which tends to reduce the hydraulic jump. The time scale of Coriolis forces is f^{-1}, that of jump-creating nonlinear forces is L/U. Hence the delay
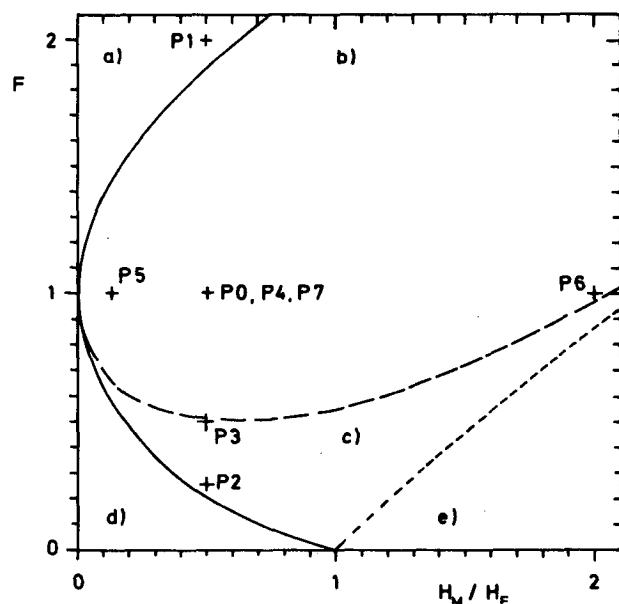

FIG. 6. Classification map of flow conditions as a function of Froude number $F = U/C$ and the relative height of the mountain H_M with respect to the height of the fluid layer at infinity, H_F, according to Houghton and Kasahara (1968). The regimes are: (a) swell without hydraulic jump, (b) jumps traveling up and downstream, (c) upstream jump traveling, downstream jump stationary, (d) dip without jumps, (e) total blocking. The flow states are indicated by the crosses for all cases according to Table 2.

is large if the Rossby number Ro $= U/(fL)$ is less than a certain number. Williams and Hori (1970) find strong delay in the generation of hydraulic jumps if the Rossby number is less than 0.1. For the cases considered in this study Ro is larger than 0.25 (see Table 2). Therefore, it is appropriate to compare the present results with the theory of Houghton and Kasahara (1968). Baines (1980) used similar arguments to justify application of the irrotational theory for determination of hydraulic blocking.

Crosses in Fig. 6 mark the state of all cases for which results have been displayed in Fig. 5. The map indicates that hydraulic jumps are to be generated for all cases except for P1 which is supercritical in the hydraulic sense. From the theory of Houghton and Kasahara (1968), the height h_{max} of the interface behind the jump has also been determined: $h_{max}/H_F = (1.61, 1.04, 1.22, 1.61, 1.29, 2.15, 1.61)$ for cases P0, P2, P3, ..., P7, respectively. For cases P0, P3, P6 and P7, the numerical solutions reflect strong hydraulic jumps in accordance with the hydraulic theory. Note that this is true in particular for P7 in spite of the rather small Rossby number (Ro $= 0.5$). Cases P4 and P5 have not yet created hydraulic jumps because the time period of the simulations shown in Fig. 5 is too small for this purpose. The computed jump height is within 20% of the predicted value for cases P0, P6 and P7. Case P2 lies at the border to subcritical flow where the gravity waves are quick enough to spread out jump-forming disturbances. Case P3 exhibits oscillations after the first hydraulic jump. Shortening the time step does not eliminate these oscillations. From the theory (Houghton and Kasahara, 1968) we know that hydraulic jumps can form only if energy is lost at the jump. Since our model does not include any friction, this energy seems to be converted into oscillating motion behind the hydraulic jump. Thus it is conjectured that these oscillations are not due to numerical deficiencies. This conjecture is corroborated by the fact that similar oscillations start to develop in cases P0 and P6 just after the hydraulic jump is fully developed.

Thus, our numerical results are consistent with the theory of hydraulic jumps. Figure 6 can be used to decide on the flow state in the limit of long times if rotational forces are sufficiently small. From the results of the present study we can conclude that this is the case for Rossby numbers larger than 0.25.

5. Influence of stable stratification in two dimensions

In the cases considered up to now, the air masses have been assumed to be neutrally stratified. For this reason, gravity waves have been restricted to waves of the frontal interface. No internal waves have been excited. Therefore, the shallow water model suits this situation well. The standard tropospheric atmosphere is, however, stably stratified. In terms of the Brunt–Väisälä frequency a typical value (e.g., see Hoinka, 1985, for

fronts in central Europe) is $N = 0.01$ s^{-1}. Near fronts this value varies considerably due to moist processes and vertical mixing, as discussed by Keyser and Anthes (1982). Above the tropopause the stability increases to much larger values. In order to investigate one effect after the other, in this study we consider the simplified case of uniform stratification with $N = 0.01$ s^{-1}. The selected initial conditions imply purely horizontal motions; therefore, stratification does not alter the quasi-stationary solution, Eqs. (1)–(3), in the absence of orographic disturbances. This can be seen from Eq. (11), in which the effect of the vertical mean temperature gradient vanishes if $w = 0$. Subsequently, the effect of stratification on frontal retardation at a mountain is discussed for a case which otherwise equals the reference case P0.

The initial conditions represent a flow which initiated impulsively from rest. Even without fronts, this causes transient mountain waves which propagate away from the mountain in all directions (Pierrehumbert and Wyman, 1985). If the front enters this transient wave field at early times it will be difficult to separate the effects of nonstationarity, stratification and frontal motion. For this reason we first simulate the transient development of the mountain waves in a case without a front in order to get a reference case against which one can compare to identify the effect of the front. Then two runs with a cold front are performed, one in which the simulation starts at $t^* = 0$ as in case P0, and one in which the simulation starts at $t^* = -1$ where the front just enters the left boundary of the computational domain. The comparison will show the effect of nonstationarity.

As displayed in Fig. 7a, the transient motion in the absence of a front causes three types of waves to be formed. The first is a transient wave on the lee side, which travels downstream in the form of a hydraulic jump. It is formed by the cold air which is advected across the mountain crest and replaces the relatively warm air initially at this position. Due to strong stratification and large mountain height, the cold air tends to penetrate below the warm air on the lee side. The second type of wave forms above the mountain and tends to become stationary after long times. The third type of wave is an upstream-propagating layer (thickness $\approx H_M$) of decelerated fluid also discussed by Pierrehumbert and Wyman (1985). When this wave reaches the inflow boundary we observe a conflict between prescribed inflow values and the internal dynamics which is responsible for the upward deflection of the isotherms at the inflow boundary. (Further tests with increased computational domains have shown that this conflict is of minor importance; the present results are used because they differ from case P0 solely by the value of N.)

Figures 7b and 7c contain the results for the two cases with the cold front. We see that the front changes the first two types of waves only little. At the upwind
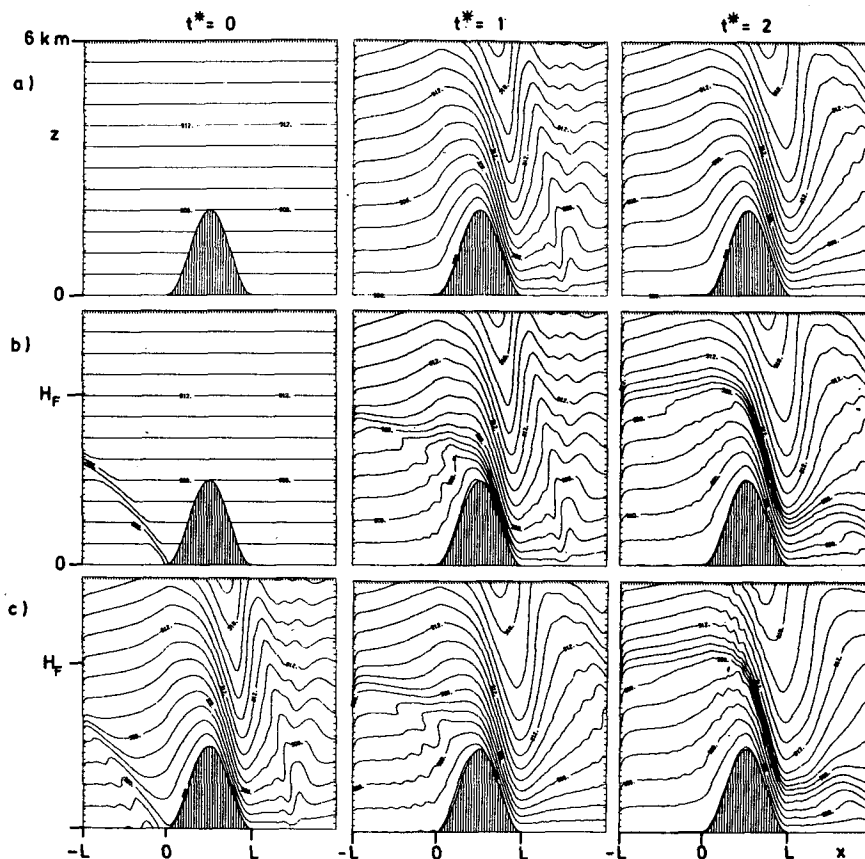
FIG. 7. Interaction of stratified flow over a mountain ridge with a cold front. The panels are plots of the isotherms (increment $\Delta\theta/2$) at a sequence of nondimensional times t^*. (a) Case without a cold front; (b) front initiated at $t^* = 0$, (c) front initiated at $t^* = -1$.

side, additional internal gravity waves arise which are trapped below the front's interface and travel upstream. The main effect of the front is an increased thickness of the layer of decelerated fluid upstream of the mountain. The differences of the results depicted in Figs. 7b and 7c are rather small. Thus, the transient of the wave motion does not seem to influence the frontal motion significantly.

From the plots of the isotherms, however, it is not easy to identify the exact position of the front because it is masked by the gravity waves. Therefore, the tracer ψ has been included in the simulation which makes the cold and warm air masses distinguishable but does not influence the dynamics of the flow (see Eq. 12). Figure 8 displays the resultant isochrones of the frontal interface for the two cases where the simulation starts either at $t^* = 0$ or at $t^* = -1$. The differences between the two cases are small. This reveals that the transient formation of gravity waves and the frontal motion are only weakly coupled by nonlinear forces for the present parameters. Therefore, the effect of stratification on fronts with the present parameters can be identified from simulations which start from initialization at $t^* = 0$. Presumably, the weak coupling originates from
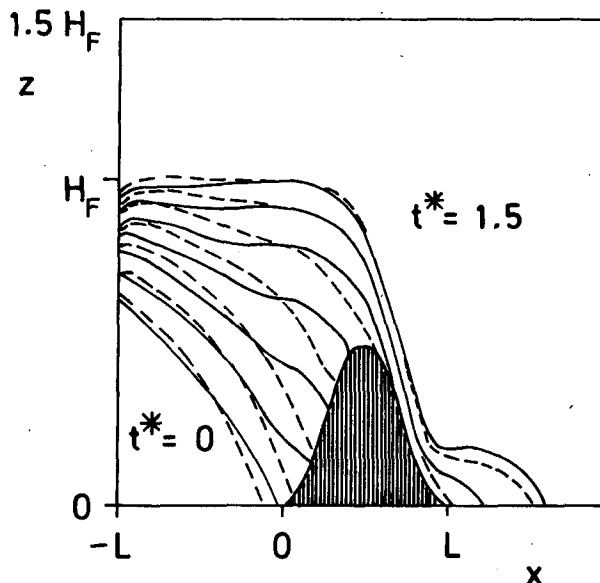

FIG. 8. Effect of stratification on the frontal interface. Isochrones of the frontal interface in stratified flow (as in Fig. 7) at times $t^* = 0$, $0.25, \ldots, 1.5$. Full curves: front initiated at $t^* = 0$; dashed curves: front initiated at $t^* = -1$.

the fact the temperature difference $\Delta\theta$ at the front is smaller than the temperature difference $H_F d\bar{\theta}/dz$, due to stratification over the front's height. The ratio of these differences equals $(HN_5)^{-1}$; it amounts to 0.25 in this case.

Comparison of the isochrones in Fig. 8 with those for case P0 in Fig. 5 shows that the front in a stratified atmosphere is more strongly retarded on the upslope side and more strongly accelerated on the downslope side than in cases without stratification. This can be explained by considering the energy balance and the spreading of waves in stratified layers.

Additional potential energy $N^2 H_M^2$ per unit mass is required to lift the air on the upslope side up to the mountain crest against the weight of the stratified fluid above. Thus, instead of N_2 now

$$N_2' = \frac{1}{2}\frac{U^2}{g' H_M + N^2 H_M^2}$$

$$= \frac{1}{2}\frac{U^2}{C^2(H_M/H_F) + N^2 H_M^2} = \frac{N_2}{1 + N_5} \quad (32)$$

controls the retardation of the front. For the present case, we have $N_5 = 2$, which explains the stronger retardation in comparison to case P0 where $N_5 = 0$.

Due to stratification, long-wave disturbances travel faster than at velocity C (Pierrehumbert and Wyman, 1985). This explains why the disturbance induced by the mountain has traveled far upstream although $C = U$. This spreading causes a flattening of the interface. The hydraulic jump which forms for case P0 gets dispersed because buoyancy forces counteract vertical motion at such a jump. As can be seen from Eq. (27), the effect of stratification will be strong in this respect even if $N_5 = F_N^2 F^2 H$ is small, since a hydraulic jump implies very large vertical velocities.

The retardation of the surface front Δ (defined by $\Delta = x_F - Ut$ where x_F is the position of the surface front at time t) takes its maximum value at $t' \approx 0.8$ when the tip of the front has reached the mountain crest. Thus, the value of Δ is about $0.3L$. This value is smaller than the value $(N/f)H_M/2$ predicted by Bannon (1984), which equals 100 km $= L/2$ in the present case. Note that Bannon's estimate for Δ implies zero retardation for $N = 0$. Presumably, the differences arise because he assumes semigeostrophic flow and small mountain heights, which we do not. Bannon's results cannot be compared directly with the present ones because he considers a mountain profile which changes with time and a front experiencing frontogenesis due to imposed horizontal stretching deformation.

6. Three-dimensional effects

In this section the influence of a simple three-dimensional mountain on the idealized cold front is investigated by applying the numerical method to a circular mountain with an axially symmetric sinusoidal height profile. The parameters selected are otherwise the same as for the reference case P0 already discussed. Cases without and with stable stratification are considered ($N = 0$ or $N = 0.01$ s^{-1}). The case with neutral stratification has also been investigated by Haderlein (1986, unpublished). For the stratified fluid, the present case is the three-dimensional variant of the case considered in section 5.

The computational domain extends over $-L \leqslant x \leqslant 2L$, $-L \leqslant y \leqslant L$, $0 \leqslant z \leqslant 1.5H_F$. The numerical method is applied with 72×48 grid cells horizontally and 30 grid cells vertically. Thus, the horizontal and vertical grid spacings are 25% larger than in the two-dimensional studies. This was necessary due to storage restrictions of the computer used. Parameter studies in two dimensions have shown that this resolution still gives sufficient accuracy.

In spite of $W = V/U = 0$, we expect strong three-dimensional effects because of equal length scales in x and y-direction [$M = 1$, see Eq. (26)]. Figure 9 contains the surface isochrones at a sequence of times and the horizontal velocity field at $t^* = 1$ near the surface for both neutral and stable stratification. For stratified fluid, the isochrones in Fig. 9 are again determined by the tracer ψ which marks the interface between the cold and warm air masses. The results show that the front is accelerated on the northern side (the y-coordinate is considered pointing north) but is retarded at the upslope side near the mountain center and even more on the southern side. At time $t^* = 1$, the maximum deformation Δ (magnitude of the displacement normal to the front with respect to the position the surface front would take without a mountain at the same time) amounts to $0.165L$ for $N = 0$, and $0.35L$ for $N = 0.01$ s^{-1}. On the downslope side, the front is accelerated and the deformation remains increasing, at least for some time.

The velocity field indicates that the flow is deflected sideways away from the mountain center. This deflection is due to gravitational forces in the cold layer as to be expected from the term $-g'\partial h_M/\partial y$ in Eq. (6). It causes the flow to split over the mountain and explains the observed form of deformation. An alternative explanation of the observed deformation can be given in terms of conservation of potential vorticity (Pedlosky, 1987, pp. 63–65). It implies that the vertical vorticity is negative (anticyclonic) for $f > 0$ whenever the vertical separation of streamlines decreases with regard to their separation at infinity (also discussed by Merkine and Kalnay-Rivas, 1976). In the present case, the vertical separation of streamlines above the mountain is reduced if gravity forces cause flow away from the mountain center. The resultant anticyclonic motion is large over the mountain but small elsewhere and thus causes the "anticyclonic deformation" of the surface front. This explanation is consistent with the explanation in terms of flow splitting, because both explanations assume gravity forces as the driving mecha-
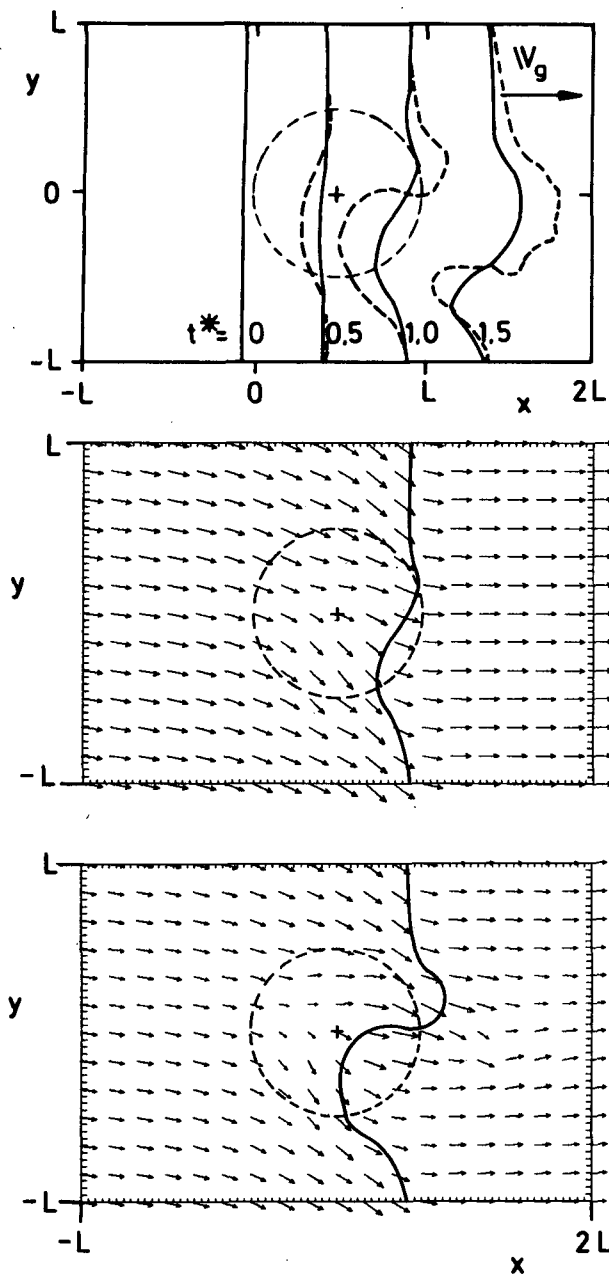
FIG. 9. Influence of a three-dimensional mountain on a cold front in neutrally and stably stratified atmosphere. The mountain is indicated by the dashed circle. Top: Surface isochrones at a sequence of nondimensional times; full curves: $N = 0$, dashed curves: $N = 0.01$ s^{-1}. Middle: Surface velocity field for $N = 0$ at $t^* = 1$; the actual position of the frontal line is indicated. Vectors are plotted for every fourth grid point. The velocity magnitude ahead of the front is 20 m s^{-1}. Bottom: Same for $N = 0.01$ s^{-1}.

nism. The results show that the retardation and acceleration effects are increased by the stratification. This is easy to understand because stable stratification enhances upslope deceleration and downslope acceleration.

The three-dimensional deformation of the front is also dependent on all those parameters controlling two-dimensional retardation. Thus it is large for a small Froude number F, for a small height aspect ratio H, and for small values of the rotational Froude number ϵ. The front's deformation is no longer invariant with respect to the velocity component V along the front. Results of further simulations (not plotted) and the results of Haderlein (1986, unpublished) show that positive (negative) values of V of order C cause comparable magnitudes of the frontal deformation, but the position of maximum deformation is shifted into positive (negative) y-direction.

7. Comparison with observed cases

In this section it will be shown that the model succeeds in describing the essential structure of observed frontal retardation. For this purpose, the model is applied to the cases displayed in Fig. 1 with parameters which are adjusted as to be as close as reasonably possible to the observed situations. Thus, we still use the idealized frontal initialization and a simplified orographic model representing merely the principal scales of the Alps. The fronts' heights and the temperature differences between warm and cold air masses are estimated from two successive midnight soundings (see Fig. 10) obtained before and after the fronts passed Munich. The fronts are clearly identifiable from the temperature changes. Also, the dewpoint temperature can be used to identify the front's height. The windfields change less significantly. Obviously, the front on 2 March 1982 is rather shallow while the front on 4 June 1986 fills virtually the whole troposphere. The temperature difference is larger in the second case. Let case A denote a simulation of the front observed on 2 March 1982, and case B the front of 4 June 1986. For case A, we see from Fig. 10a that the temperature has dropped on average by 6 K over a height interval of 4.5 km. Being aware that these are rough estimates, we specify $\Delta\theta = 6$ K and $H_F = 4.5$ km for case A. From Fig. 10b we obtain the values $H_F = 9$ km and $\Delta\theta = 7$ K for case B. The geostrophic wind component normal to the front is estimated from the movement of the front at the surface according to Fig. 1: $U = 12$ m s^{-1} for case A, and $U = 10$ m s^{-1} for case B. The wind component along the front is set to $V = 40$ m s^{-1} for case A and $V = 15$ m s^{-1} for case B. In view of the vertical shear (see Fig. 10), this value is very uncertain. The orography of the Alps is represented by an ellipsoidal mountain with length 1000 km and width 200 km and a maximum height $H_M = 2.5$ km. These parameters are summarized in Table 3. The computational domain covers a square with 2000 km side lengths and extends vertically up to $z_t = 11$ km, which approximates the height of the tropopause. The finite-difference grid includes 40 grid cells in each horizontal direction and 30 grid cells vertically. In order to allow for periodic lateral boundary conditions, the front has to be parallel to the
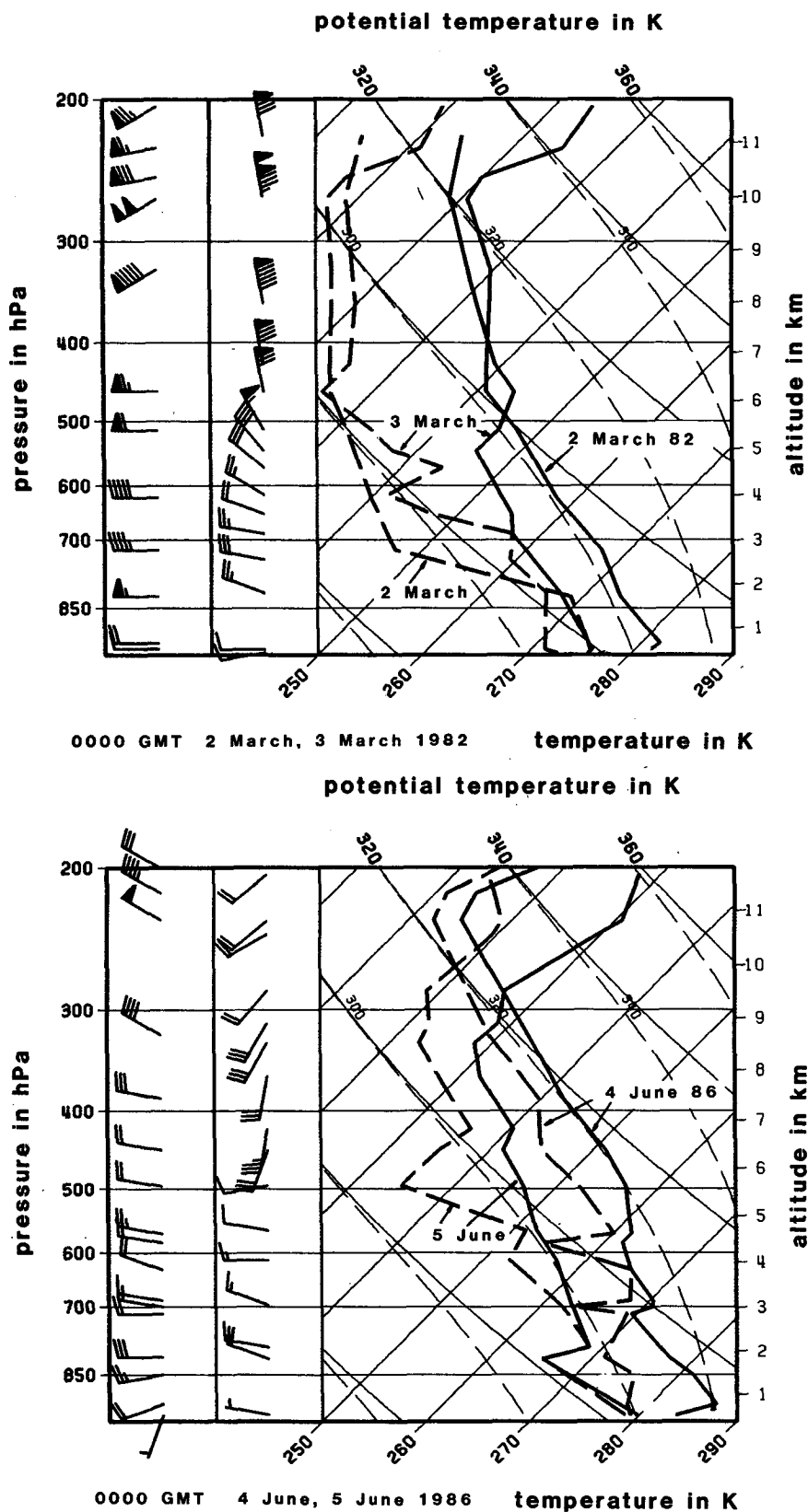
FIG. 10. Skew T–log p diagram from the rawinsonde Munich (Germany). Full curves: temperature; dashed curves: dewpoint temperature; wind vectors in standard notation. (a) Top: 2–3 March 1982; (b) Bottom: 4–5 June 1986.

TABLE 3. Parameters for comparison with observed cases. Case A models the front on 2 March 1982; case B the front on 4 June 1986. In both cases: $g = 10$ m s^{-2}, $f = 10^{-4}$ s^{-1}, $\theta_0 = 300$ K, $\rho_0 = 1.2$ kg m^{-3}, and $N = 0$ for runs A1 and B1, $N = 0.01$ s^{-1} for runs A2, A3, B2 and B3.

	Physical parameters							
Case	H_M (km)	L (km)	H_F (km)	$\Delta\theta$ (K)	U (m s^{-1})	V (m s^{-1})	C (m s^{-1})	R (km)
A	2.5	200	4.5	6	12	40	30	300
B	2.5	200	9	7	10	15	45.8	458

	Nondimensional numbers for stable stratification											
	ϵ	H	F	G	N_1	N_2	N'_2	N_3	$10^5 N_4$	N_5	F_N	Ro
A	0.667	1.8	0.4	0.013	0.24	0.144	0.064	0.833	4.87	1.25	2.083	0.6
B	0.436	3.6	0.218	0.013	0.109	0.086	0.041	0.636	2.89	1.07	2.5	0.5

inflow boundary of the computational domain. However, in case A (see Fig. 1a) the front approaches the Alps from approximately the northwest while it comes from nearly due north in case B. Therefore, the mountain is rotated by 30° relative to the line of the front in the model for case A.

For each case three runs have been performed:

- A1 and B1: with neutral stratification and a mountain having a sinusoidal height profile (as in the two-dimensional cases) along both principle axes of the ellipsoidal mountain domain.
- A2 and B2: with stratification ($N = 0.01$ s^{-1}) and the same sinusoidal height profiles.
- A3 and B3: with the same stable stratification but a mountain which has constant height H_M throughout the ellipsoidal domain and slopes down to zero height over one grid interval outside this domain. (The orographic model used in A3/B3 suits the steep Alps better than the sinusoidal profile and is still simple.)

The results of the simulations are given in Fig. 11. Isochrones of the surface front are plotted at a sequence of times. The time increments (3 h) correspond to the analysis shown in Fig. 1a. The full curves are the isochrones for cases A3 and B3, which exhibit the largest effects. For the other cases, the resultant surface front is plotted only for the final time (15 h after model initialization). In the simulations of case A the front reaches the northwest corner of the mountain about 5 hours after initialization. Ten hours later, the front has not yet reached the mountain center but has by far passed the western edge. To the first order, this agrees with the observations shown in Fig. 1a. For case B, the simulation indicates that this front, too, is strongly retarded initially. This was not expected from the large-scale analysis reported in Fig. 1b. However, the front soon climbs over the mountain, and at the final time of the simulation the front has passed the mountain and the remaining deformation of the surface front is decreasing. Obviously, the time resolution of Fig. 1b (24 h) is too coarse to resolve the simulated retardation.

The maximum (positive and negative) deformation of the surface front has been determined from the computed isochrones (by comparing with the surface front which would result without mountains). These deformations are plotted versus time in Fig. 12 for all runs. In the same manner, the observed retardation of the surface front on 2 March 1982 can be measured from Fig. 1a by comparing to fictitious frontal lines which are parallels to that given in Fig. 1a at 0000 UTC 2 March 1982 at distances tU with the given time differences t and $U = 12$ m s^{-1}. These values are indicated by circles in Fig. 12. As can be seen, the cases with the smooth sinusoidal mountain profile (A1, B1) exhibit rather small values for the deformation of the front. Stable stratification (A2, B2) does enhance the deformation but not to the observed magnitude. The deformation is strongly enhanced, however, if the sinusoidal mountain is replaced by a mountain with constant height and steep slopes (A3, B3). The results for case A3 compare very well with the observed retardation. A time shift of 2 hours would yield even smaller differences. For case B, Fig. 12 clearly shows that the computed front tends to become less deformed at late times. It appears reasonable that the remaining deformation is no longer notable from standard synoptic observations one day after the front has arrived at the northern side.

From the estimated input parameters we can evaluate the relevant nondimensional characteristic numbers (see Table 3) and expect

- semigeostrophic motion for case B because both N_1 and N_2 are small; however, notable departure from semigeostrophy for case A because N_1 is not very small.
- strong retardation of the foot of the front at the mountain because N_2 and N'_2 are small in both cases.
- Davies' solution gives physically meaningful results only for the initial period ($t^* < 1$) because N_3 is larger than π^{-1} in both cases, indicating a mountain profile which is steep in comparison to the frontal slope.
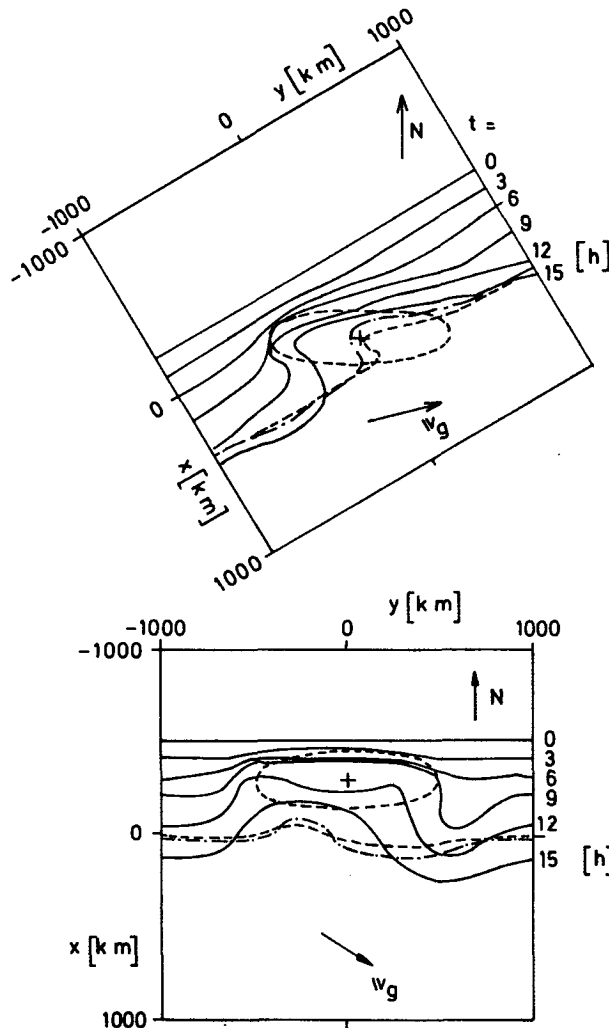- hydrostatic flow, because N_4 is small in both cases.

FIG. 11. Above: Simulated isochrones of the surface coldfront on 2 March 1982 (cases A1, A2, A3; top) and 4 June 1986 (cases B1, B2, B3; bottom). The domain of the mountain is given by the dashed ellipsoidal curve. The cross identifies the center of the mountain. The arrow indicates the direction of the geostrophic wind in the warm air mass. Dashed curves: cases A1 and B1 at $t = 15$ h; dash-dotted curves: cases A2, B2 at $t = 15$ h; full curves: cases A3, B3 at time intervals of 3 h.

• generation of hydraulic jumps in case A but no jumps in case B, as can be deduced from Fig. 6 for the estimates of F and H given in Table 3; Figure 6 is applicable because the Rossby number is sufficiently large.

• strong effects of stratification because N_5 is of order unity in both cases.

• due to differences in the ratio V/C, the wind behind the front is westerly in case A but more easterly in case B; this explains some of the differences in the shape of the surface front.

These estimates are qualitatively consistent with the results of the observations and the simulations. The

results show that not only are the frontal parameters important, but so is the direction from which the front approaches the elongated mountain.

8. Summary and conclusions

The effect of simple mesoscale mountains on an idealized cold front in a neutrally or stably stratified atmosphere is studied using a three-dimensional model. The model accounts for inertia, gravity and Coriolis forces over high mountains. Many further effects like friction, surface heating, cloud processes and more complex initial and boundary conditions, as well as realistic orography, are still to be investigated. The present numerical method offers the potential for such extended studies. In particular, it can be applied to nonhydrostatic situations. However, it appears important for understanding to consider such effects step by step.

The solutions of the present method have been compared with results from the semigeostrophic shallow water model by Davies (1984). Further comparisons with a numerical solution of the shallow water equations by Haderlein (1986, unpublished) have been performed and are to be reported elsewhere. The comparisons have demonstrated that the numerical method used to integrate the model equations is well suited to the present purpose in spite of the discontinuous initial and boundary values. Also, the appearance of hydraulic jumps consistent with previous theories supports the validity of the numerical method.

A scale analysis shows that the semigeostrophic approximation is valid if the characteristic numbers N_1 and N_2 are both small (see Table 1). For neutral stratification ($N_5 \ll 1$) the flow is approximately hydrostatic if N_4 is small. For fronts parallel to a two-dimensional mountain ridge, the velocity ratio V/U does not influence the frontal deformation. As shown by Davies (1984), the effect of orography on a cold front is determined by ϵ and N_3. For small rotational Froude numbers ϵ, the mountain effect is felt far upstream. For large values of the steepness parameter N_3, the front is strongly retarded and the semigeostrophic model breaks down after some time.

The semigeostrophic model cannot account for important flow effects like the upwelling of the foot of the front on the windward mountainside or the formation of hydraulic jumps. Moreover, the shallow water model does not account for dynamic effects of the warm air mass above and ahead of the cold front. Such effects are important in stably stratified air and for small-scale orography with nonhydrostatic flow.

If the conditions imply large deviations from the semigeostrophic equilibrium, important characteristic numbers are: N_2, deciding on whether the kinetic energy suffices to let the front just jump over the mountain; and the Froude number F controlling the spreading of disturbances by gravity waves up and down-
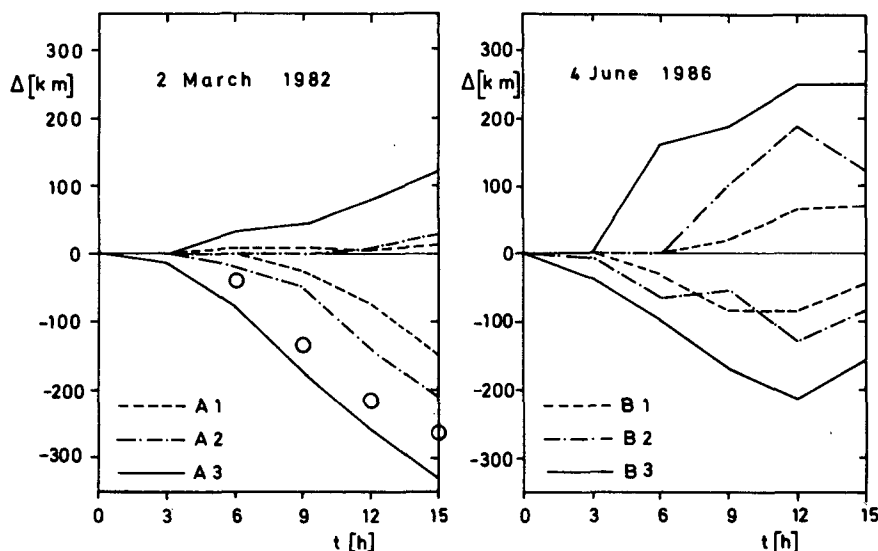
FIG. 12. Maximum surface-front deformation Δ in positive and negative direction for the simulations of the front on 2 March 1982 (cases A1, A2, A3; left) and 4 June 1986 (cases B1, B2, B3, right). The circles correspond to the observed values deduced from Fig. 1a. Dashed curves: cases A1 and B1; dash-dotted curves: cases A2, B2; full curves: cases A3, B3.

stream. For Froude numbers of order one and sufficiently high mountains, hydraulic jumps are formed in the interface between cold and warm air masses. Coriolis forces do not seem to be important in this respect as long as the Rossby number Ro = F/ϵ is larger than 0.25. A front requires additional kinetic energy to overcome stable stratification with little retardation. Moreover, stable stratification disperses hydraulic jumps. The effect of stratification on orographic retardation of a cold front is large if N_5 is large. The inverse effect of the front on mountain waves ahead of the front has been found to be small. The maximum retardation of fronts for high mountains and nongeostrophic conditions differs considerably from the result of Bannon (1984).

For a given mesoscale mountain, the results imply strong retardation if the front is shallow, if the temperature difference between warm and cold air is large, if the velocity normal to the front is small and if the atmosphere is very stably stratified. For a given front, the retardation is strong if the mountain is high and steep.

In three dimensions, the front experiences anticyclonic deformation. This effect is a consequence of splitting of the flow above the mountain by gravity forces. Stable stratification enhances this distortion. The maximum deformation of the surface front is larger than in two-dimensional cases. The position of the maximum distortion depends on the velocity component parallel to the front.

The model quantitatively explains the magnitude of retardation of cold fronts at the Alps as observed by Steinacker (1983). It was found that the retardation

was very sensitive to stratification and to the steepness of the mountain profile. Also, the relative angle of incidence of the front on the elongated mountain is important. The front's deformation is larger if the front approaches the Alps from the northwest than if the front comes from due north.

REFERENCES

Baines, P. G., 1980: The dynamics of the southerly buster. *Australian Meteor. Mag.*, **28**, 175–200.

Bannon, P. R., 1984: A semigeostrophic model of frontogenesis over topography. *Beitr. Phys. Atmos.*, **57**, 393–408.

Blumen, W., C. Hartsough and B. Gross, 1986: Frontal interaction with orography. *Scientific Results of the Alpine Experiment (ALPEX)*, GARP Publ. Ser. 27, WMO/TD-No. 108, Vol. II, p. 437–444. [Obtainable from the Secretariat of the WMO, C.P. No. 5, CH-1211 Geneva 20, Switzerland.]

Bougeault, P., 1983: A nonreflecting upper boundary condition for limited-height hydrostatic models. *Mon. Wea. Rev.*, **111**, 420–429.

Buzzi, A., and S. Tibaldi, 1978: Cyclogenesis in the lee of the Alps: A case study. *Quart. J. Roy. Meteor. Soc.,* **104,** 271–287.

Clark, T. L., 1977: A small-scale dynamical model using a terrain-following coordinate transformation. *J. Comput. Phys.,* **24,** 857–878.

Davies, H. C., 1984: On the orographic retardation of a cold front. *Beitr. Phys. Atmos.,* **57,** 409–418.

——, 1986: Diagnostic studies of meso-α scale flow on the alpine northside. *Scientific Results of the Alpine Experiment (ALPEX),* GARP Publ. Ser. 27, WMO/TD-No. 108, Vol. II, p. 425–436.

Godske, C. L., T. Bergeron, J. Bjerknes and R. C. Bundgaard, 1957: *Dynamic Meteorology and Weather Forecasting.* Amer. Meteor. Soc., p. 612.

Hoinka, K. P., 1985: On fronts in central Europe. *Beitr. Phys. Atmos.,* **58,** 560–571.

——, 1986: On the diagnosis of a cold front observed during ALPEX. *Scientific Results of the Alpine Experiment (ALPEX),* GARP Publ. Ser. 27, WMO/TD-No. 108, Vol. II, p. 444–453.

Houghton, D. D., 1969: Effect of rotation on the formation of hydraulic jumps. *J. Geophys. Res.,* **74,** 1351–1360.

——, and A. Kasahara, 1968: Nonlinear shallow fluid flow over an isolated ridge. *Comm. Pure Appl. Math.,* **21,** 1–23.

Keyser, D., and R. A. Anthes, 1982: The influence of planetary boundary layer physics on frontal structure in the Hoskins-Bretherton horizontal shear model. *J. Atmos. Sci.,* **39,** 1783–1802.

Klemp, J. B., and D. R. Durran, 1983: An upper-boundary condition permitting internal gravity wave radiation in numerical meso-scale models. *Mon. Wea. Rev.,* **111,** 430–444.

Long, R. R., 1972: Finite-amplitude disturbances in the flow of inviscid rotating and stratified fluids over obstacles. *Ann. Rev. Fluid Mech.,* **4,** 69–92.

Merkine, L.-O., and E. Kalnay-Rivas, 1976: Rotating stratified flow over finite isolated topography. *J. Atmos. Sci.,* **33,** 908–922.

Pedlosky, J., 1987: *Geophysical Fluid Dynamics.* Second ed., Springer-Verlag, 710 pp.

Pichler, H., and R. Steinacker, 1986: On the synoptics and dynamics of orographically induced cyclones in the Mediterranean. *Scientific Results of the Alpine Experiment (ALPEX),* GARP Publ. Ser. 27, WMO/TD-No. 108, Vol. I, p. 245–250.

Pierrehumbert, R. T., and B. Wyman, 1985: Upstream effects of mesoscale mountains. *J. Atmos. Sci.,* **42,** 977–1003.

Schumann, U., and H. Volkert, 1984: Three-dimensional mass- and momentum-consistent Helmholtz-equation in terrain following coordinates. *Notes on Numerical Fluid Mechanics,* Vol. 10, W. Hackbusch, Ed., Vieweg, 109–131.

Smith, R. B., 1986: Mesoscale mountain meteorology in the Alps. *Scientific Results of the Alpine Experiment (ALPEX),* GARP Publ. Ser. 27, WMO/TD-No. 108, Vol. II, p. 407–423.

Smolarkiewicz, P. K., 1984: A fully multidimensional positive definite advection transport algorithm with small implicit diffusion. *J. Comput. Phys.,* **54,** 325–362.

Steinacker, R., 1981: Analysis of the temperature and wind fields in the Alpine region. *Geophys. Astrophys. Fluid Dyn.,* **17,** 51–62.

——, 1983: The first ALPEX-SOP cold front on 2 March 1982. *ALPEX Preliminary Scientific Results,* WMO Geneva, GARP-ALPEX No. 7, p. 87–96. [Obtainable from the Secretariat of the WMO, C.P. No. 5, CH-1211 Geneva 20, Switzerland.]

——, 1984: Airmass and frontal movement around the Alps. *Riv. Met. Aeronaut.,* **43,** 79–83.

Volkert, H., and U. Schumann, 1986: Development of an atmospheric mesoscale model–Setting up the version in terrain following coordinates. *Notes on Numerical Fluid Mechanics,* Vol. 13, D. Rues and W. Kordulla, Eds., Vieweg, p. 375–382.

Williams, R. T., and A. M. Hori, 1970: Formation of hydraulic jumps in a rotating system. *J. Geophys. Res.,* **75,** 2813–2821.